

SEARCH FOR SOMETHING

by

Joaquin Emilio Siado Castañeda

A DISSERTATION

Presented to the Faculty of

The Graduate College at the University of Nebraska

In Partial Fulfilment of Requirements

For the Degree of Doctor of Philosophy

Major: Physics and Astronomy

Under the Supervision of Professor Daniel Claes

Lincoln, Nebraska

July, 2020

# SEARCH FOR SOMETHING

Joaquin Emilio Siado Castañeda, Ph.D.

University of Nebraska, 2020

Advisers: Dan Claes and Aaron Dominguez

my abstract

COPYRIGHT

© 2020, Joaquin Emilio Siado Castañeda

my rights

*For you*

## ACKNOWLEDGMENTS

Many people has contributed to make this work possible that it is impossible to name them all.

thank you all.

---

## Table of Contents

---

<b>List of Figures</b>	<b>ix</b>
<b>List of Tables</b>	<b>xi</b>
<b>1 Introduction</b>	<b>1</b>
<b>2 The LHC Accelerator and the CMS Experiment</b>	<b>2</b>
2.1 The LHC Accelerator . . . . .	2
2.2 The CMS Experiment . . . . .	4
2.2.1 The Muon Chambers . . . . .	8
2.2.2 The Hadronic Calorimeter . . . . .	8
2.2.3 The Electromagnetic Calorimeter . . . . .	9
2.2.4 The Tracker Detector . . . . .	9
2.2.4.1 Silicon Strips . . . . .	9
2.2.4.2 Pixel Detector . . . . .	9
2.2.4.3 The trigger . . . . .	10
<b>3 The SM and BSM Theories</b>	<b>11</b>
<b>4 Event generation, simulation and reconstruction</b>	<b>12</b>

<b>5 Search for the particle</b>	<b>13</b>
<b>6 More on the Analysis?</b>	<b>14</b>
<b>7 Module Production for the Phase I CMS Pixel Detector Upgrade</b>	<b>15</b>
7.1 The CMS Forward Pixel Detector Phase I Upgrade . . . . .	16
7.2 Module Production at UNL . . . . .	19
7.2.1 Visual Inspections . . . . .	19
7.2.2 IV Test . . . . .	23
7.2.3 Gluing . . . . .	23
7.2.4 Wirebonding . . . . .	24
7.2.5 Encapsulation . . . . .	26
7.2.6 Electrical Test of a Fully assembly Module . . . . .	27
7.2.6.1 IV Test . . . . .	30
7.2.6.2 Pretest . . . . .	30
7.2.6.3 Pixel Alive . . . . .	31
7.2.6.4 Trimming Test . . . . .	32
7.2.6.5 PH Optimization . . . . .	34
7.2.6.6 Gain Pedestal . . . . .	37
7.2.6.7 Scurve Test . . . . .	37
7.2.6.8 Bond Bonding Test . . . . .	38
7.2.6.9 Summary . . . . .	39
<b>8 Beam Test of the RD53 chip for CMS Pixel Detector Upgrade Phase 2</b>	<b>44</b>
<b>9 Conclusions</b>	<b>46</b>
9.1 Analysis . . . . .	46

9.2 Phase 1 . . . . .	46
9.3 Beam Test . . . . .	46
<b>References</b>	<b>47</b>

---

## List of Figures

---

2.1	The CERN acceleration <i>facilities</i>	3
2.2	CMS detector	4
2.3	LHC luminosity	5
2.4	CMS cross sectional view	7
2.5	CMS detector coordinate system	7
2.6	Pixel detector	10
7.1	Simulated performance comparison of previous and current	17
7.2	Layout of the upgraded and old pixel detectors.	18
7.3	Half disks and half cylinder	18
7.4	UNL module assembly workflow	20
7.5	Photograph of a BBM and HDI.	21
7.6	Photograph of the visual inspection and IV test station.	21
7.7	Visual inspection of a bare module.	22
7.8	Visual inspection of a HDI.	22
7.9	IV test of BBM	24
7.10	Gluing and encapsulation set up	25
7.11	Gluing result	25

7.12	wirebonder machine . . . . .	26
7.13	Wirebonding process . . . . .	26
7.14	Encapsulation materials . . . . .	27
7.15	Encapsulation results . . . . .	28
7.16	Fully assembly Module . . . . .	29
7.17	Testing set up . . . . .	29
7.18	IV results of a module . . . . .	30
7.19	Programable ROC and working point . . . . .	32
7.20	Pixel alive test . . . . .	32
7.21	Faulty pixel alive test . . . . .	33
7.22	Trim test turn on . . . . .	34
7.23	Trim test Trim bits . . . . .	35
7.24	Trim test final . . . . .	36
7.25	PH vs Vcal . . . . .	36
7.26	PHOffset and PHScale scan . . . . .	37
7.27	Gain pedestal test . . . . .	38
7.28	Scurve test . . . . .	39
7.29	Bond bonding test. . . . .	40
7.30	Module assembly over time. . . . .	41
7.31	Module grade over time. . . . .	42
7.32	Pixel unit cell. . . . .	43
8.1	Test beam setup . . . . .	44
8.2	Test beam setup . . . . .	45

---

## List of Tables

---

7.1 Module grade . . . . .	40
----------------------------	----

## CHAPTER 1

---

### **Introduction**

---

Talk about particle physics in general and the organization of the documents

## CHAPTER 2

---

### The LHC Accelerator and the CMS Experiment

---

In the 1960s Peter Higgs [3] and others [4, 5] put up the finishing touches on a theory combining three of the four fundamental forces and explainign how gauge bosons acquire mass. Nowadays this theory is known as the Standard Model (SM) of particles physics. It predicted the existence of several particles which were discovered in following decades. However, one particle was proving to be elusive, the so-called Higgs bosson. With this in mind the European Council for Nuclear Research (CERN) started plans to build an accelerator large enough and with the sufficient energy to prove the existance of the Higgs boson. Hence, the Large Hadron Collider (LHC) was born.

## 2.1 The LHC Accelerator

The large hadron collider, shown in figure 2.1, is the biggest particle accelerator built by mankind to date. It has 27 km in circumference and is located in the French-Swiss border outside of Geneva, Switzerland [1]. Using the previous installations as the large electron-positron collider the LHC can be operated in  $pp$  mode or heavy ion mode. In  $pp$  mode<sup>1</sup>, the LHC accelerates two beams of protons in opposite directions

---

<sup>1</sup> Only  $pp$  collision and considered in this document.

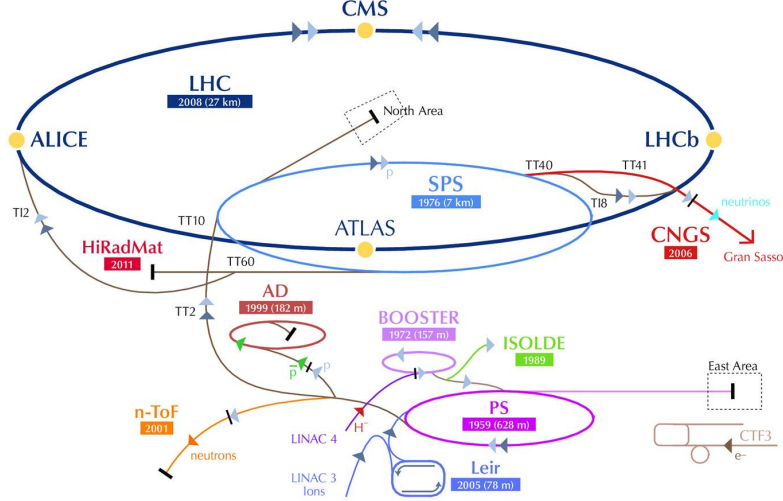


**Figure 2.1:** The CERN acceleration facilities showing the location of the four main experiment as well as the acceleration process[need ref].

until they collide at different points. In its initial physics run in 2011 and 2012, the LHC collided protons every 50 ns, at a center of mass energy of 7 Tera electron Volts (TeV), reached a peak luminosity of  $7.7 \times 10^{33} \text{ cm}^{-2} \text{ s}^{-1}$ <sup>2</sup>, and delivered an integrated luminosity of  $\approx 25 \text{ fb}^{-1}$  to each of its two general purpose experiments, ATLAS and CMS. The analysis of this data yielded many physics results including the discovery of the Higgs boson published in 2013 [6, 7]. During the following years the collider's luminosity was increased and its bunch crossing time reduced allowing for the Higgs boson properties to be measured.

Four experiments were designed and built along the 27 km of the LHC ring. Two of them, A Toroidal Large Apparatus (ATLAS) [8] and the Compact Muon Solenoid (CMS) [9] are large multipurpose experiments. The third experiment is LHCb [10], which is specifically dedicated to study B-meson physics, the last experiment ALICE [11], A Large Ion Collider Experiment, is dedicated to investigate heavy ion collisions.

<sup>2</sup> The LHC design luminosity is  $10^{34} \text{ cm}^{-2} \text{ s}^{-1}$

## 2.2 The CMS Experiment

The compact muon soleinod, shown in figure 2.2 is one of the two multipurpose experiment at the LHC. The two main goals of the CMS experiment was to measure SM parameter with high precision as well as to test different physics theories beyond the standard model (BSM), i.e. SUSY, Dark matter and Dark energy, etc. The first goal has been achieve,

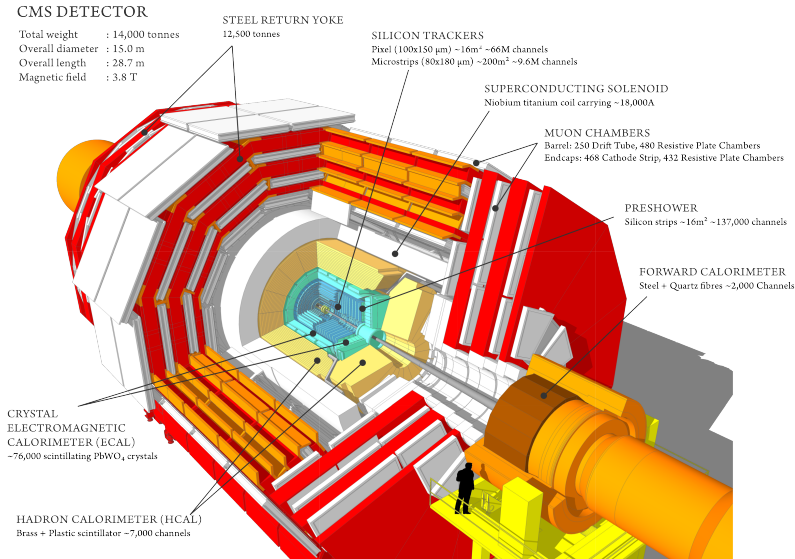


**Figure 2.2:** CMS detector [14].

during its running years CMS has collected more than  $160 fb^{-1}$  of data. This has yielded numerous phisics results luminosity a total of aspect To achieve its goal

CMS is one of two general purpose experiments at the LHC and it is located at Point 5 as shown in Fig. 1.2. It is designed to take data using both proton-proton and ion-ion collisions. The main physics goals are the search for the SM Higgs boson and physics beyond the SM, heavy quarks, and heavy ion physics. CMS has to fulfill several requirements [15]:

Good muon identification and momentum resolution over a wide range of mo-

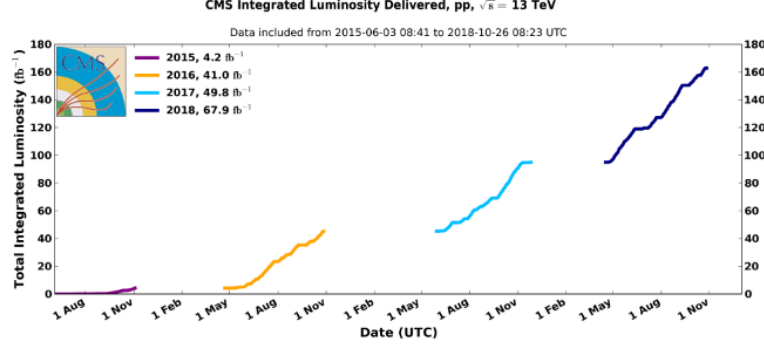


**Figure 2.3:** Total integrated luminosity delivered by the LHC machine to the CMS experiment from 2015 to 2018 [15]

menta in the pseudorapidity 3 region  $|\eta| < 2.5$ , good dimuon mass resolution (âLÍ 1 and the ability to determine unambiguously the charge of muons with  $p < 1 \text{ TeV}/c$ . Good charged particle momentum resolution and reconstruction efficiency in the inner tracker. Efficient triggering and offline tagging of D âZs and b-jets, requiring pixel detectors close to the interaction region. Good electromagnetic energy resolution, good diphoton and dielectron mass resolution (âLÍ 1 of photons and/or correct localization of the primary interaction vertex, ď 0 rejection and efficient photon and lepton isolation at high luminosities. Good transverse missing energy E T miss and dijet mass resolution, requiring hadron calorimeters with a large hermetic geometric coverage ( $|\eta| < 5$ ) and with fine lateral segmentation. The requirements above led to the detector design shown in Fig. 1.3. Ideally, the detector shape would be spherical for best hermeticity but this is almost impossible technically. A cylindrical shape therefore is chosen to achieve very good geometrical coverage and include a magnetic solenoid for particle momentum measurements.

CMS comprises several sub detectors (see Fig. 1.3). An assembled part of the CMS experiment in SX5 underground is shown in Fig. 1.4. The sub detectors from the innermost to outermost are the inner tracker (silicon strips and pixels) â

the electromagnetic calorimeter 3 6  $\pm$  the hadronic calorimeter and

The origin of the CMS coordinate system is at the interaction point, the y-axis pointing vertically upward, and the x-axis pointing radially inward towards the center of the LHC ring. The z-axis points along one of the beam direction (towards the Jura mountains). The azimuthal angle  $\phi$  is measured from the x-axis in the x-y plane. The polar angle  $\theta$  is measured from the z-axis. These coordinates will also be used later in this thesis.

**1.3.1 Magnet** As mentioned before, CMS requires a high performance of the muon system and a momentum resolution of 10% of a superconducting solenoid and a magnet yoke. The solenoid is 13 m long and has an inner diameter of 6 m. It contains the tracker and calorimeters. The magnetic field inside the solenoid is 4 T while in the yoke it is 2 T. The bending direction within the solenoid is opposite to the one in the magnet yoke, as shown in Fig. 1.5. This provides a longer path for the energetic muons, increasing the precision of muon momentum measurements.

**1.3.2 Inner tracking system** The expected charged particle flux as a function of the distance to the interaction point determined the design of the inner tracker system. At a distance of 4 cm a flux of up to 100 MHz/cm<sup>2</sup> is expected. The innermost part of the tracker will be exposed to very high radiation doses, with time causing severe radiation damage to the tracker material. The radiation dose is proportional to  $1/r^2$ , where r is the radius of the tracker layer. The expected radiation dose and hadron fluence in radial layers of the CMS tracker are shown in Table 1.2 for different radii. It is worth mentioning that a few Grays of dose is lethal for human. One of the main challenges is to operate the tracker in such a harsh environment for an expected lifetime of 10 years at the full LHC luminosity  $10^{34} \text{ cm}^{-2} \text{ s}^{-1}$ . The radiation hardness, granularity and speed requirements favored devices based on silicon technology.

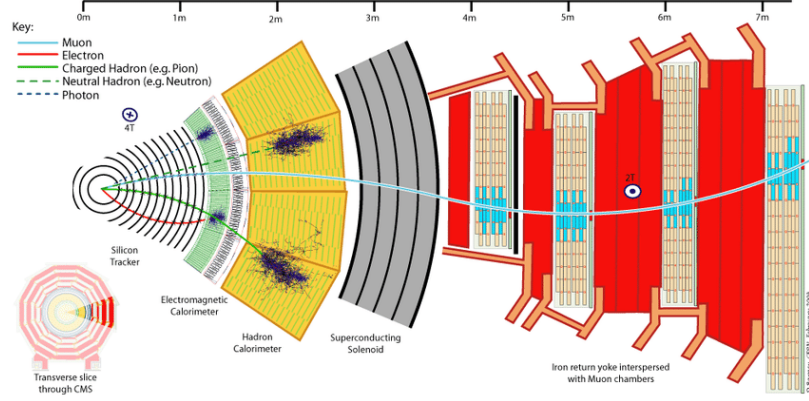


**Figure 2.4:** CMS cross sectional view.

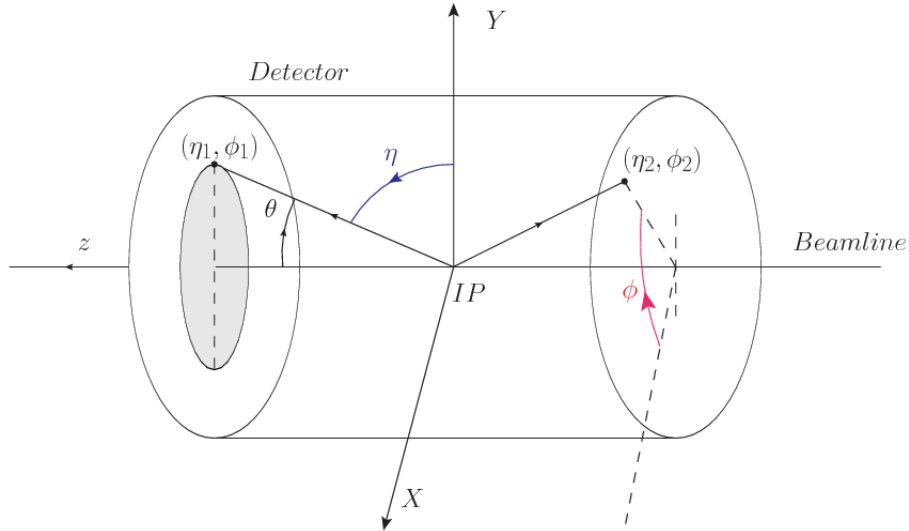


**Figure 2.5:** CMS detector coordinate system [18].

Describe from the outside the CMS experiment subdetector are: the muon chambers, the hadronic calorimeter, the Electromagnetic calorimeter, the superconducting solenoid, and the tracker detector which is composed of the silicon strips and the pixel detector.

### 2.2.1 The Muon Chambers

Muons have a relatively long lifetime of 2.2  $\mu$ s. They interact weakly with matter and are not stopped by the calorimeters where they deposit some of their energy. The CMS muon detectors therefore are the outermost sensitive devices in the experiment [21]. The muon detectors are divided into a barrel and two end cap regions. The system utilizes three different technologies: drift tubes (DT) in the barrel region, cathode strip chambers (CSC) in the end- cap region and resistive plate chambers (RPC) in both barrel and end-cap regions. The RPCs provide a trigger signal while DT and CSC detectors can reconstruct the muon trajectory and momentum. The muon system covers the region  $|\hat{\eta}| < 2.4$ . The muon system is important for muon identification. For transverse momenta below 200 GeV the muon identification relies on the inner tracker.

### 2.2.2 The Hadronic Calorimeter

Similar to the ECAL the aim of the hadronic calorimeter (HCAL) is to measure the energy and the direction of strongly interacting particles and jets as well as missing transverse energy. The CMS HCAL [20] surrounds the ECAL. It has a sandwich structure of brass absorbers and plastic scintillators. The reason for choosing these materials is that they have smaller radiation lengths which minimize multiple scattering for traversing muons. The hadron barrel and end caps cover the range  $|\hat{\eta}| < 3$  with higher granularity. There are additional scintillators installed inside the muon barrel layer and steel-quartz fibers in the very forward region providing overall pseudorapidity coverage of  $|\hat{\eta}| < 5$ .

### 2.2.3 The Electromagnetic Calorimeter

An electromagnetic calorimeter (ECAL) is used to measure the energy and direction of electrons, photons, and jets. Measurements with very high precision are required. The CMS ECAL is made of lead-tungstate ( $\text{PbWO}_4$ ) crystals. The high density of the crystals ( $8.2 \text{ g/cm}^3$ ) leads to a short radiation length and narrow showers, which allow for a compact calorimeter inside the solenoid that is fast, has fine granularity, and is radiation resistant [19]. The ECAL pseudo-rapidity coverage is  $|\hat{\eta}| < 3$ . Particle induced scintillation light is detected by silicon avalanche photodiodes (APDs) in the barrel region and vacuum phototriodes (VPTs) in the end cap region.

### 2.2.4 The Tracker Detector

#### 2.2.4.1 Silicon Strips

#### 2.2.4.2 Pixel Detector

Being the innermost detector in CMS, the pixel detector works in a high radiation environment but, due to its excellent design and construction, it performed well during the initial CMS run. It provided two or more hits per track, allowing secondary vertex identification of long-lived objects. The pixel detector is composed of two parts, the barrel (BPix) and a disk at each end, denominated Forward pixel detector (FPix), as showing in figure 2.6. The BPix is made of three layers located at 4.3 cm, 7.2 cm, and 11.0 cm from the interaction point respectively. The FPix has two layers, one at 34.5 cm and the other at 46.5 from the interaction point. This thesis will focus on the FPix, the part of the detector where UNL has made major contributions in the last **two** three decades.

The original FPix, also known as phase 0, was populated by 672 modules of 100

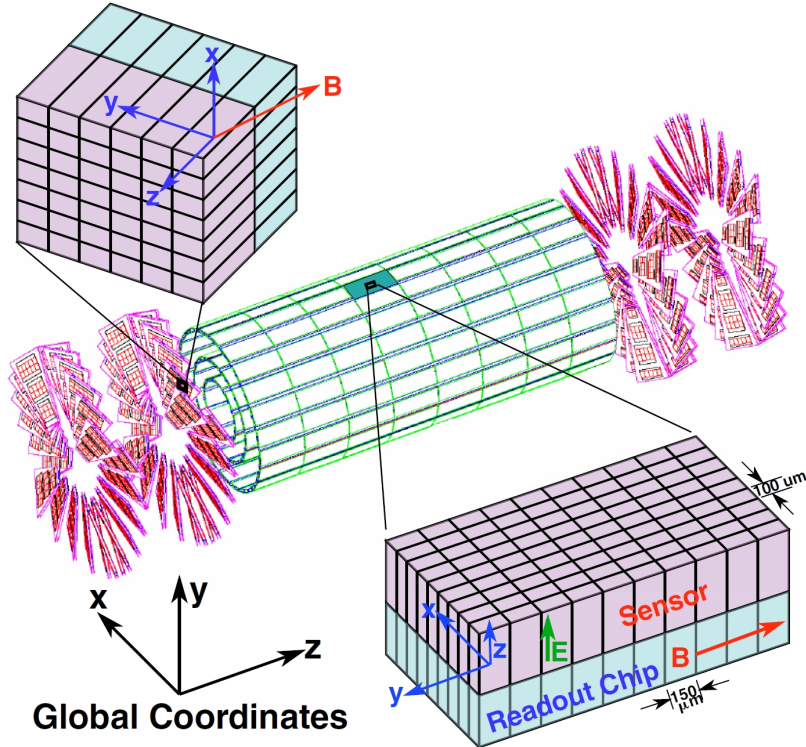


**Figure 2.6:** Pixel detector.

by  $100 \mu m$

#### 2.2.4.3 The trigger

The CMS trigger system has a two step decision system after which events will be recorded. The first trigger level, Level 1, decreases the event rate from 40 MHz to 100 kHz. The Level 1 is implemented in hardware and its decision takes 3.2  $\mu$ s. This level requires information from the calorimeters and the muon detectors. The second level is known as High Level Trigger (HLT). The HLT is implemented in software. It uses the data from all CMS subdetectors. The event rate is reduced to 150 Hz at this level.

## CHAPTER 3

---

### The SM and BSM Theories

---

It is the most succedfull scintific theory ever written. Proposed in the 1960s the standard model of particles physics has been successful in describing many phenomena of the particle world

unanswered question of sm. First goal achieve but still many other questions to solve

## CHAPTER 4

---

### **Event generation, simulation and reconstruction**

---

Description of event generation and simulation

## CHAPTER 5

---

### Search for the particle

---

Data analysis details

## CHAPTER 6

---

### More on the Analysis?

---

More?

## CHAPTER 7

---

### Module Production for the Phase I CMS Pixel Detector Upgrade

---

As discussed in chapter 2, radiation has a big impact on the CMS pixel detector causing damage to its components throughout its lifetime, therefore this detector needs to be periodically upgraded. The first version of the detector was known as phase 0, it was installed in 2008 and became fully operational in 2010 after a magnet failure caused a delay in the LHC original starting date. In 2017 the pixel detector was replaced during the phase I pixel upgrade. From 2013 to 2106 the University of Nebraska, high energy group (UNL-HEP) played a major role in assembling and testing, which then became part of the forward region of the pixel detector. The next generation of the pixel detector, the phase II upgrade, is projected to take place in 2025 when the current detector will be reaching its radiation limits and its performance will be deteriorated. In this chapter we describe why the phase 0 pixel detector needed an upgrade and the main changes done to it. We also present a description of the module assembly and testing process at UNL. Some of the steps in the process will be highlighted and in detailed as they were my contributions to the production campaign.

## 7.1 The CMS Forward Pixel Detector Phase I Upgrade

how many modules 768 or 672.

The phase 0 detector performed well during the LHC run I, taking data at a peak luminosity close to  $7 \times 10^{33} cm^{-2}s^{-1}$  and energy of 8 TeV. This data was used in many physics analysis including the discovery of the Higgs boson published in 2013. But after a few years of operation the pixel detector started to degrade due to radiation damage, causing an increase of fake rates as well as loose on resolution. Moreover, for run II the LHC physics program planned three major updates: to more than double its luminosity with successive increment until it reaches its peak of  $2 \times 10^{35} cm^{-2}s^{-1}$ , to increase the center of mass energy to 13 TeV and finally to its design value of 14 TeV, reduce the bunch crossing from 50 ns to 25 ns hence increasing the amount of pile up per interaction. As it was designed the phase 0 pixel detector could not withstand such collision conditions. Therefore plans began to design and construct a new and improved detector that could perform effectively in the new LHC running conditions. Figure 7.1 shows a comparison in performance of the previous (top) and the current (bottom) pixel detector under different luminosity and pile-up conditions.

$\tau\tau$ .  $\mathcal{DT}$

For the current pixel detector a new layer was added to the barrel and the forward region, as shown in figure 7.2. The three FPix endcap disks are located at 29.1 cm, 39.6 cm, and 51.6 cm from the interaction point. Compared to the old FPix, the innermost disk is 4.4 cm closer to the interaction point. This provides a four-hit coverage for tracks ranging up to  $\pm 2.5$  in pseudorapidity. To reduce the extra material added by the extra layer of the pixel detector a lightweight support was used, a CO<sub>2</sub> cooling system was adopted, and inactive materials were moved away

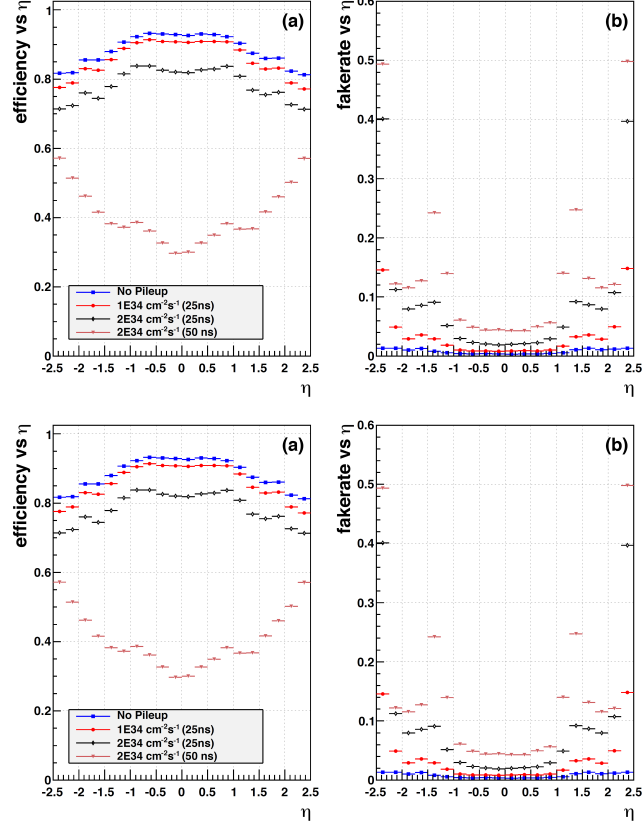


**Figure 7.1:** Simulated performance of the previous pixel detector (top) and current (bottom) under different conditions using a  $t\bar{t}$  sample: a) track-finding efficiency; b) fake rate. Conventions are the same for both plots, considering zero pileup (blue squares), average pileup of 25 (red dots), average pileup of 50 (black diamonds), and average pileup of 100 (magenta triangles) [find figure](#). [16].

from the tracking area. Figure ?? shows the amount of material needed for both the old and the current pixel detector as a function of eta.

In general the geometry of the current FPix is similar to the old detector. The three disks are vertically divided into half-disks, and are composed of inner and outer disks. This allows for easy assembly and disassembly for repairs when necessary. Each of these three disks are mounted on half cylinders, which also contains the CO<sub>2</sub> cooling tubes and the readout electronics as shown in figure 7.3. Each half disk contains 56 modules bringing the total number of modules for the FPix to 672. One

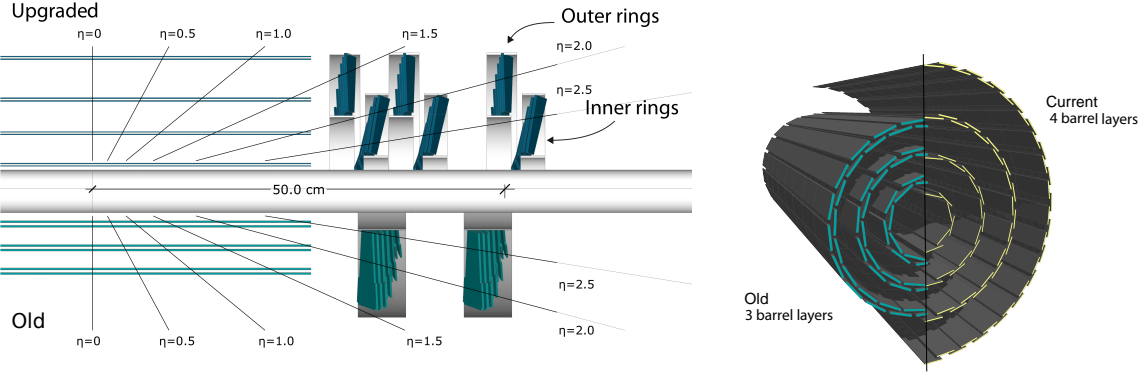


**Figure 7.2:** Layout and comparison of the layers and disks in the upgraded (Phase I) and old (Phase 0) pixel detectors [16].

key difference between the old and current detector is the use of one single module type in a 2x8 array. This made easier the installation compared to the old detector.

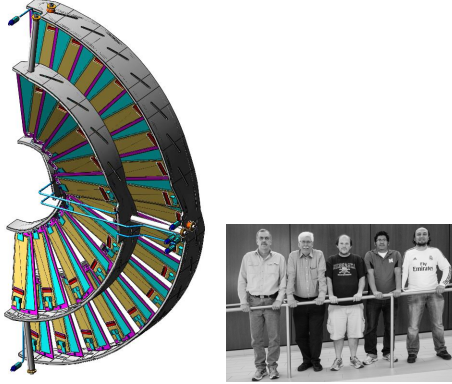


**Figure 7.3:** Half disks and half cylinder for the forward pixel detector [16].

Modules are composed of 16 read out chips (ROCs) and each ROC is form by 4160 pixels of 100mm x 150 mm. **improve of module and readout** Modules are mounted on the inner and outer half disks and not attached to the half cylinder. This allows damaged modules to be replaced without having to disassembly the half cylinder. The modules in the inner ring are rotated by 12 degrees towards the interaction point to improve resolution in both the azimuthal and radial direction.

## 7.2 Module Production at UNL

The module production for the FPix was a joint effort among several US institutions. University of Nebraska and Purdue University were assembly sites, Kansas University was x-ray testing site, and modules were finally tested and incorporated to the disks in the silicon laboratory detector at FermiLab.

The assembly process workflow at UNL was designed to follow a pipeline-like structure as shown in figure 7.4. This allows for different batches of modules to be going through it at different stages without stopping the workflow. Following is a short description of the tests and procedures performed during the production in the UNL silicon Lab. Special emphasis will be made in IV test, visual inspection and electrical test, the stages where the author of this work made a lot of contributions **improve**.

### 7.2.1 Visual Inspections

The UNL-HEP group assembly workflow started upon receiving two components: a Bare Bonded Module (BBM) and a High Density Interconnect (HDI), see figure 7.5. The first stage of the module production was a visual inspection on these components to ensure they were in good conditions and able to continue into the production pipeline.

To get a good view of such a small components a powerful microscope with magnification of **confirm**, an attached camera, and LED ring illumination was used. A photograph of the set up, also referred to as probe station, is shown in figure 7.6. The entire set up was connected to a vacuum line to secure these component in place and avoid any damage during the visual inspection. BBMs were received in a gel pack while HDIs were usually received in their modules carriers. BBMs and HDIs were

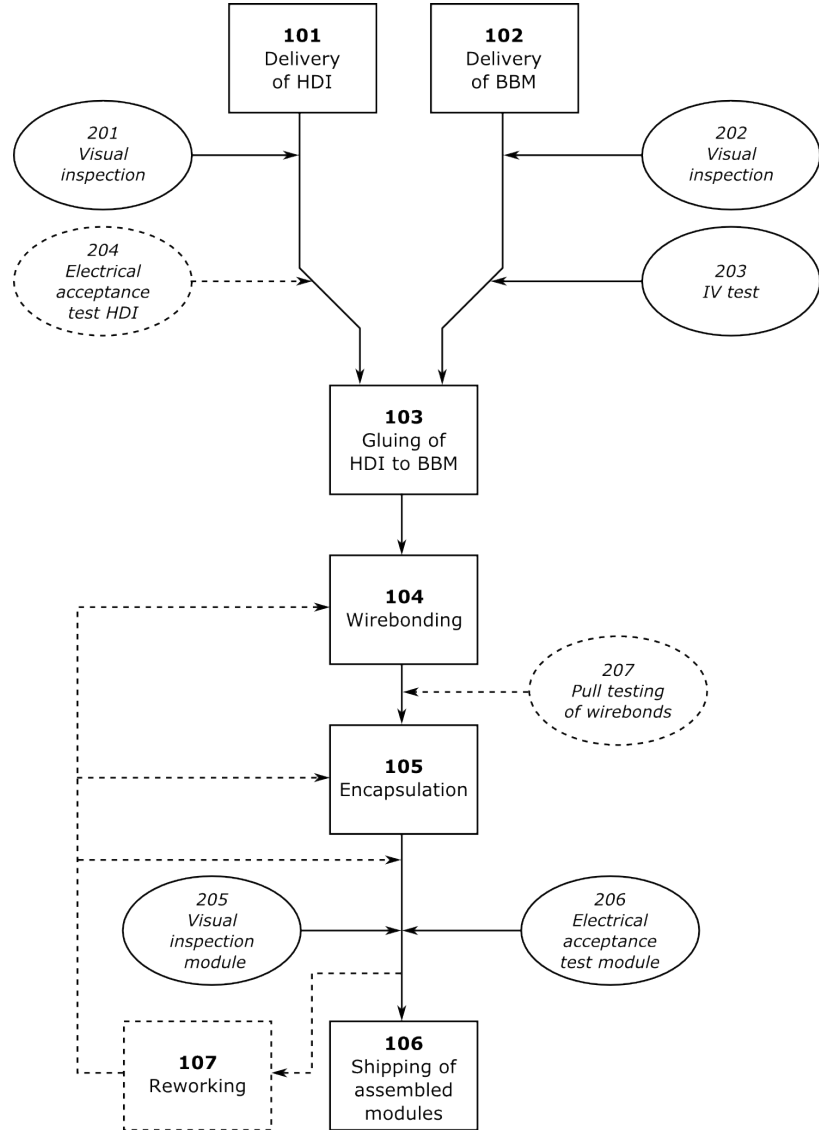


**Figure 7.4:** UNL module assembly workflow. Dashed lines represent occasional quality testing and reworking procedures [17].

then moved into the probe station using a vacuum pen and taking the appropriate safety precaution: ESD wristband, gloves, face mask, etc.

During visual inspection BBMs were scanned for unusual features or sign of damage, special attention was given to the high voltage connection and bond pads. Figure 7.7 shows different parts of four different modules where defects on three of them could be observed. Some of these defects, bottom right figure, caused the module to be re-

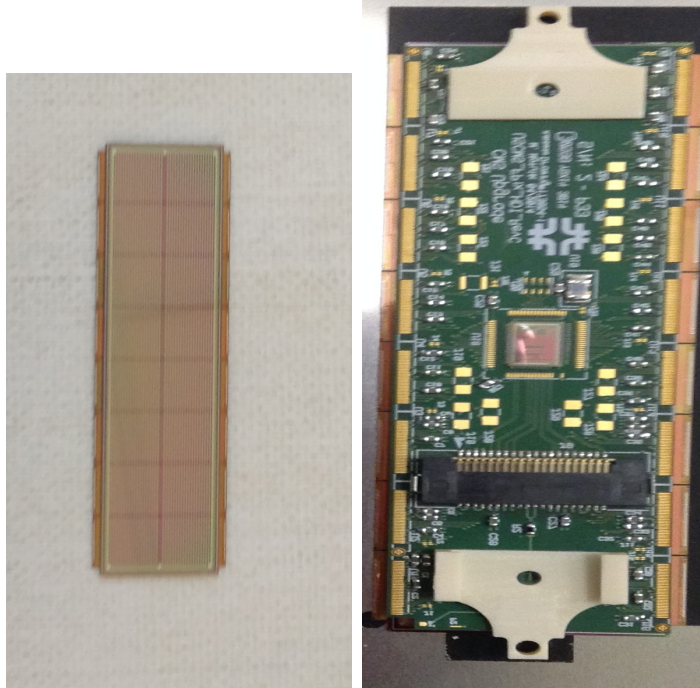


**Figure 7.5:** Photograph of a BBM (left) and HDI (right) as received by the UNL-HEP group.

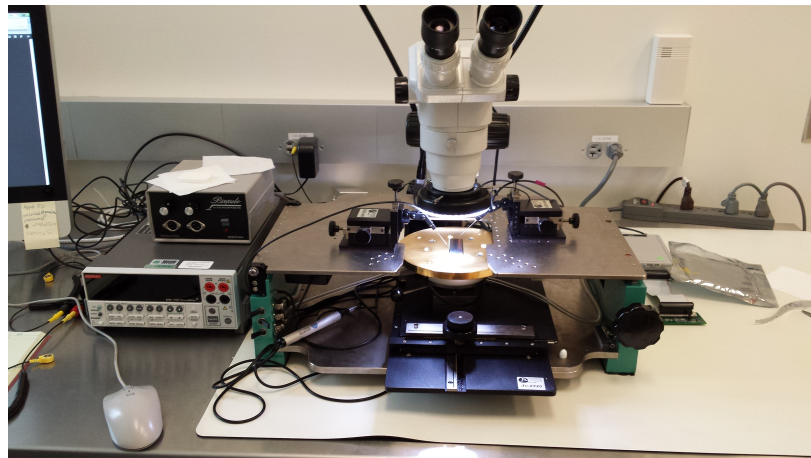


**Figure 7.6:** Photograph showing a BBM under the microscope during a visual inspection. This station also served as IV test stand.

jected immediately while others, bottom figures, will still undergo an IV test. While for the HDI the bond pads of the 16 ROCs, the wirebonds of the tbm, and the address pads were carefully checked. Figure 7.8 shows the TBM wirebonds as well as

the bondpads of a ROC in a HDI.

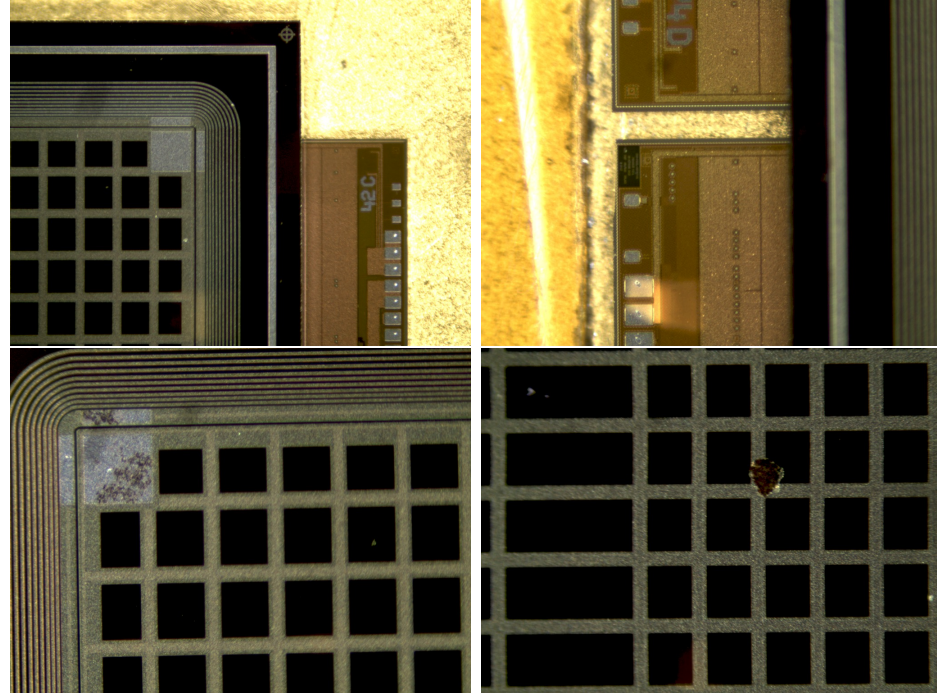


**Figure 7.7:** Photograph of the visual inspection of a BBM showing few of the things observed during a visual inspection: A good module (top left), chipped ROC (top right), scratches on the high voltage connection pad (bottom left), and scratch on the middle of a ROC (bottom right)

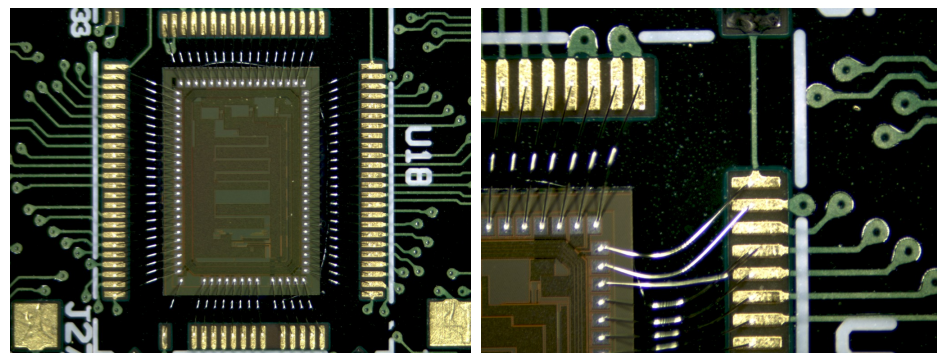


**Figure 7.8:** Photograph of the visual inspection of an HDI showing the wirebonds of the TBM. Left: good wirebonds connections, right: bent TBM wirebonds, these wires had to be straightened before encapsulation.

Figures 7.7 and Fig. 7.8 also show a trend that was observed throughout the entire production phase. In general more unusual features and damage were observed

in BBMs than on HDI. This was because BBM were delivered directly from the production company to our lab while HDIs were first delivered to the Fermi National Laboratory (FermiLab) where they were preliminary tested and inspected before they arrive at our testing facilities.

### 7.2.2 IV Test

After both BBM and HDI have successfully passed the visual inspection the BBM continues to the probe station for a current vs voltage (IV) test. The test uses the fact that the sensor behaves like a diode. During operation a potential difference is applied to the sensor to draw the electrons created by a charge particle passing through the sensor towards the bump bond to be collected. If this potential difference is too small not all electron will be collected in time and if it is large the sensor could break. This potential difference is known as a depletion voltage. The IV test is meant to find the operating range, a voltage where all the electron could be collected and the sensor will not break, for a given module (sensor). Figure 7.9 (left) shows the position of the probes to perform an IV on a BBM and figure 7.9 (right) shows IV results for a BBM in good operating condition.

### 7.2.3 Gluing

The gluing routine was carefully designed to perfectly match the HDI and BBM bond-pads, in preparation for the wirebonding. This stage of the production was done using a custom made gantry, *AGS15000 Series Gantry*, fabricated by Aerotech [20]. It offered translational motion in 3D as well as rotation in x-y (gantry table) plane. A camera was attached to the gantry head allowing the user to monitor the entire process. This camera was of particular importance during the development and

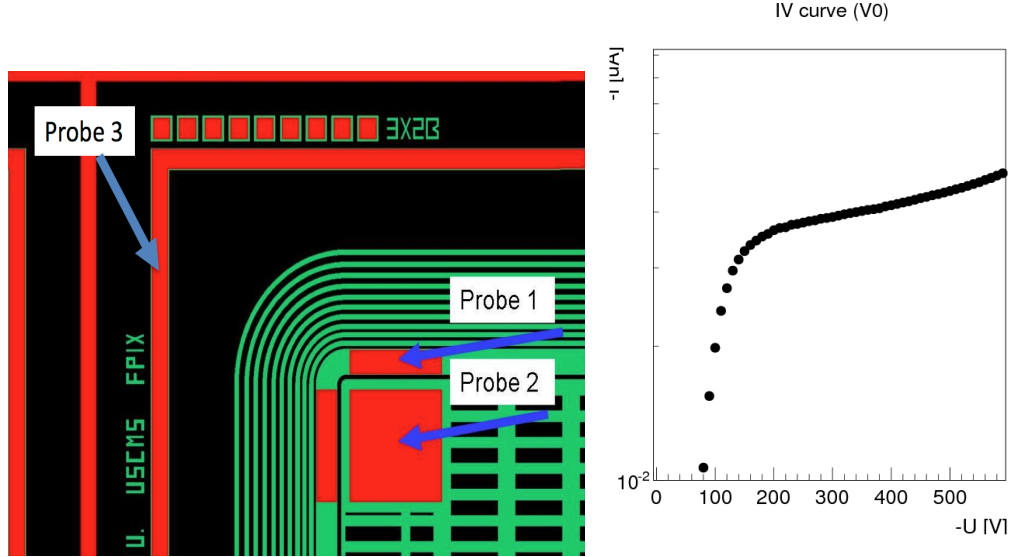


**Figure 7.9:** Left: Probe position for an IV test on a BBM. Probe 2 is high voltage, probe 3 is ground, and probe 1 was not used [17]. Right: IV test results for a good BBM. The depletion voltage for this module is around [confirm with right picture](#).

improvement of the gluing and encapsulation routine. A video showing the gluing routine in action can be watched at [19] and a full description of the gluing routine and procedure can be found in [18]. Figure 7.10 shows the gantry with the different tools used to glue a HDI on a BBM. The final product after the process is completed can be seen in Fig. 7.11.

#### 7.2.4 Wirebonding

After an HDI is glued to a BBM the next step in the assembly process is to make electrical connection between them. To this end, a wirebonder machine, Delvotec 56XX shown in figure 7.12. The first step in wirebonding was to find the position of the 35 bondpads for both the HDI and the BBM for all 16 ROCs. These positions were then fed into a custom made program to make the process automated. Using

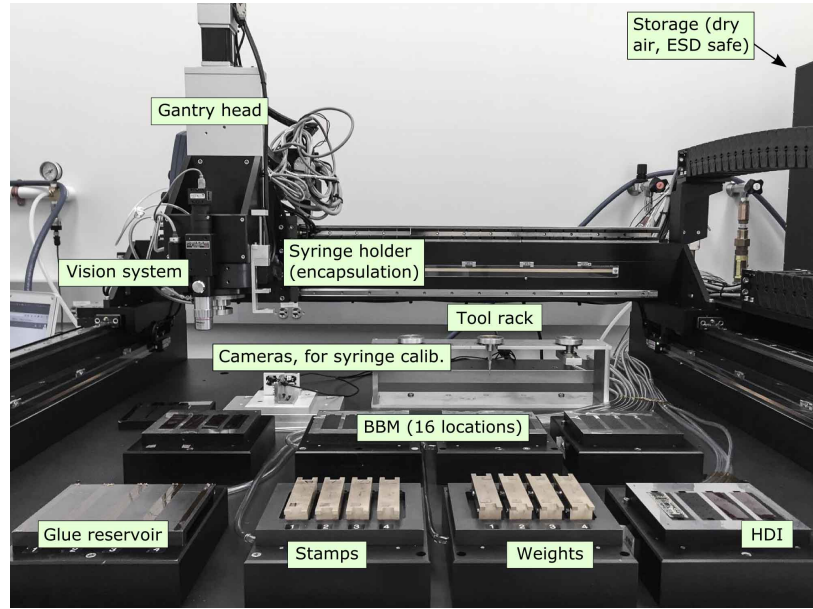


**Figure 7.10:** Photograph of a gantry used for gluing and encapsulation showing different parts of the set up and tools.

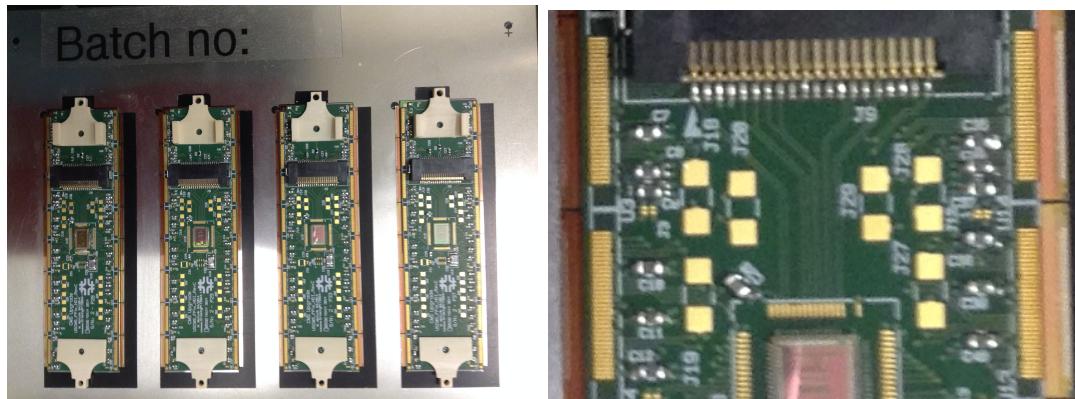


**Figure 7.11:** HDI glued on top of a BBM. For a batch of four modules (top) and zoom in view to note the almost perfect alignment between the HDI and BBM bondpads.

this software the wirebonder used aluminium wires of  $25\ \mu\text{m}$  in diameter to make the connection between the HDI and the BBM

Figures 7.13left, shows the wirerebinding process for a batch of two modules. The setup allowed for a maximum of 4 modules to be wirebonded in parallel. The program could also be modified to make repairs in individual wirebonds. And 7.13right, shows a close up view of the wirebonds of a ROC in a module.



**Figure 7.12:** Wirebonding set up [find good picture of the wirebonder](#).

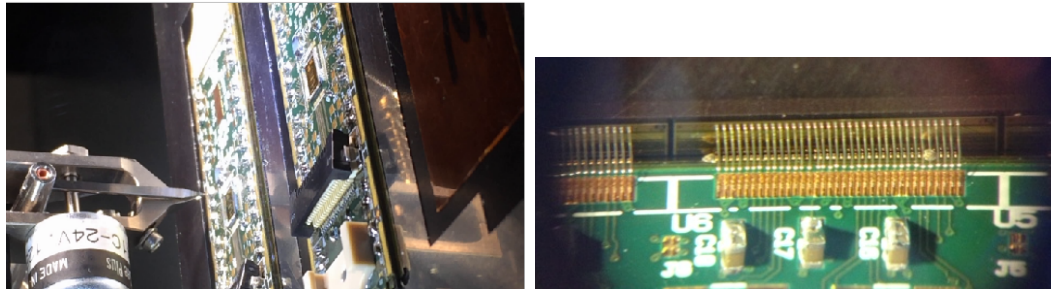


**Figure 7.13:** Left: Wirebonder in action with a batch of two modules. Right: Close up look at a ROC after wirebonding [\[24\]](#).

### 7.2.5 Encapsulation

The final step in manufacturing a module is to protect (cover) the wirebonds with an encapsulant, wirebond encapsulation. This procedure is necessary to ensure that the wirebonds are secure at both HDI and BBM ends. The set up and the equipment used is the same as for gluing showed in figure 7.10. Additional materials needed for this step are shown in figure 7.14.

A material suitable for this task must be radiation hard and lightweight among

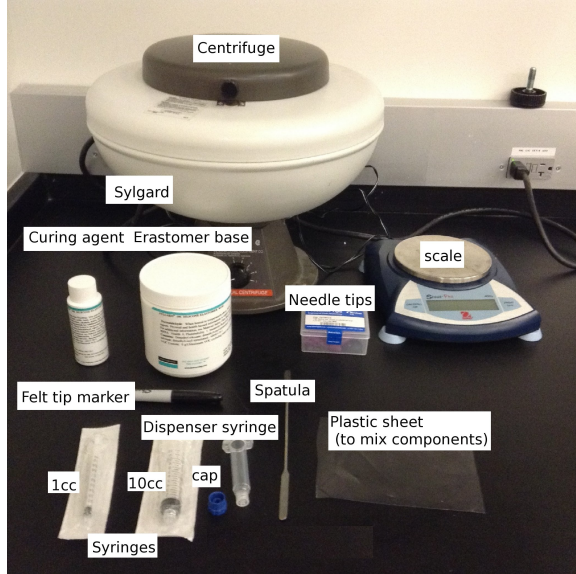


**Figure 7.14:** Wirebonds encapsulation materials [17].

other properties. After testing different material and alloys we settle on *Silgard 186*, a mixture of two-component encapsulant. Erastomer (10 cc) and elastomer (1 cc) base and curing agent respectively. The components then, were mix together using a centrifuge and place in a syringe for dispensing. There are three components that need encapsulation, HDI and BBM bond pads, TBM wirebonds, and high votage pads. Figure 7.15 shows a module after its different components have been encapsulated. Note how all bond foots and pads are fully covered as needed [18].

### 7.2.6 Electrical Test of a Fully assembly Module

A manufactured module can be seen in Figure 7.16, it is then visually inspected and mark as ready for electrical test [at the end of previous session?](#). The electrical test, hereon fulltest, of fully assembly modules is done using the *pXar* software framework, written by the CMS FPix collaboration. More information on *pXar* can be found in [22]. The objective of the *Fulltest* is to ensure that all 16 ROCs were functional and have good performance. For this purpose a suit of several tests were designed

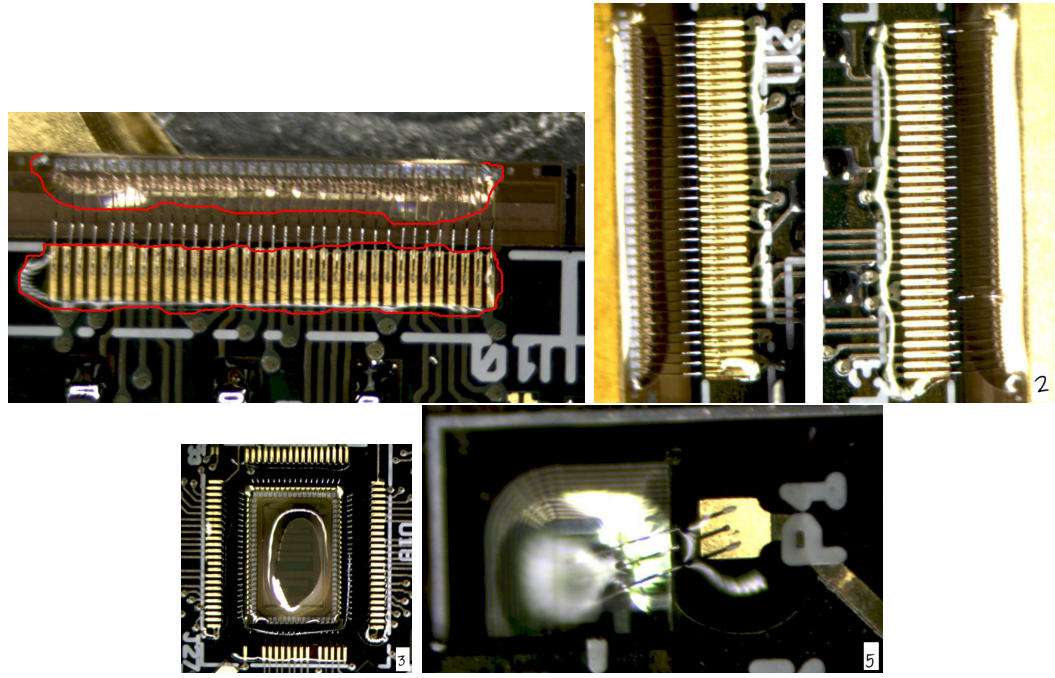


**Figure 7.15:** Wirebonds encapsulation of the components of a module. Top left, roc used as reference, the boundaries of the encapsulant are enhanced with red lines for better visibility. Top right, two ROCs on two different modules side by side, b) encapsulation of TBM, c) encapsulation of the high voltage pad.

and developed, the software is flexible in the sense that we could execute a single test just by calling its name or we could execute them all with a single command *Fulltest* with the exception of the IV test. The *Fulltest* at UNL was done using the set up showing in figure 7.17 at a temperature of  $17^{\circ} C$  and using a depletion voltage of  $-150 V$ . The set up allowed us to test up to 4 modules in parallel using a software called *ElComandante* [?] written specifically for this purpose. The modules are connected via flex cables to adapter cards which convert the data into SCSI format. Each adapter card is connected to a digital test board and the data is finally transferred to a computer via an USB cable. The temperature inside the colbox was controlled by a chiller.

The following section subsections? give a short description of the most *important* tests a module has to surpass as well as the output of these test. A full list of the

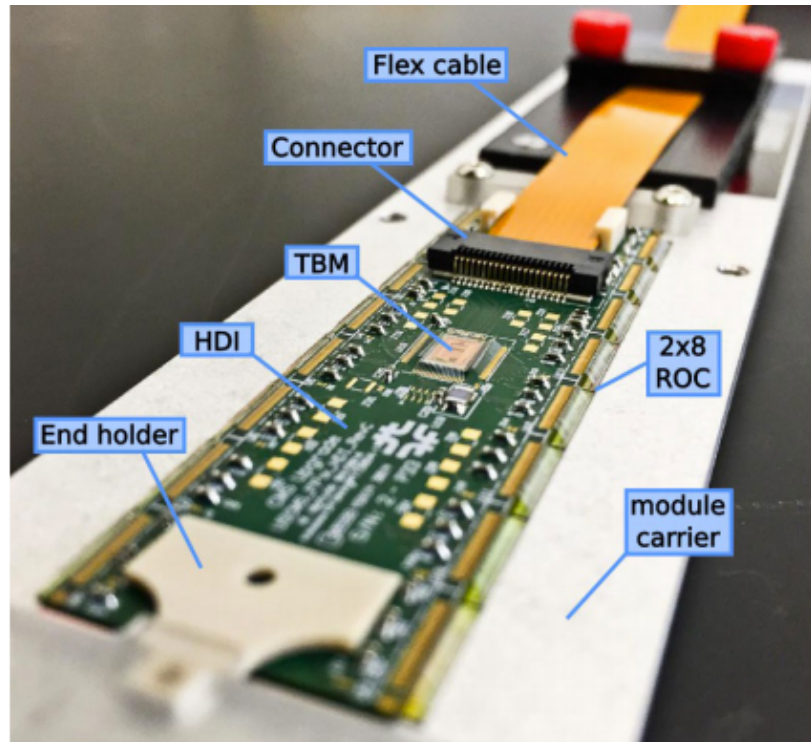


Figure 7.16: Fully assembly Module

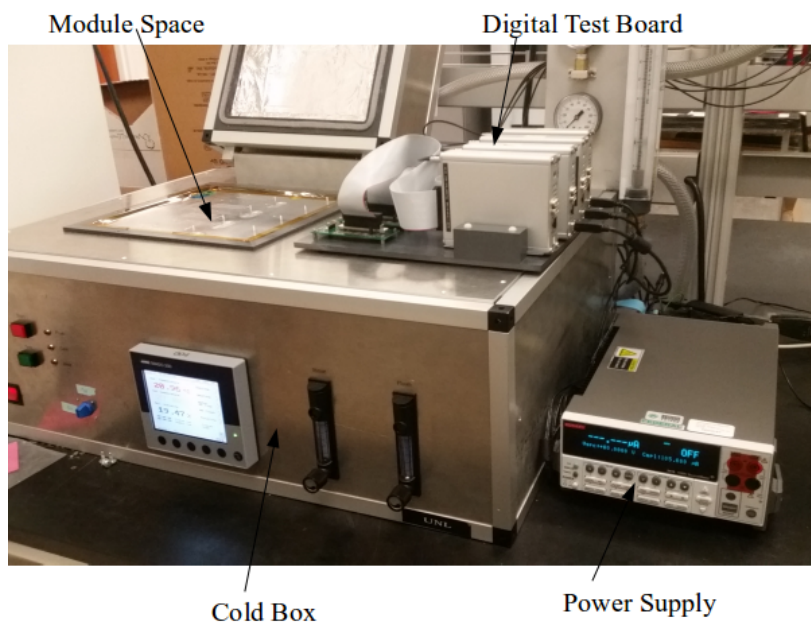
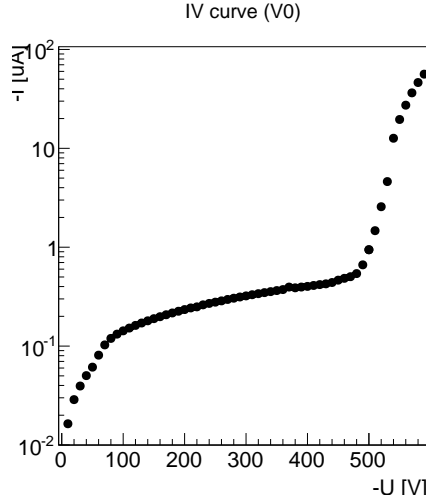


Figure 7.17: Fully assembly module testing set up

tests, a comprehensive description of them, and a [description](#) of their purpose can be found in [23] and references therein. After the *Fulltest* of modules was completed some were shipped to Kansas university for X-ray testing and the rest were shipped to FermiLab for testing at  $-10^\circ C$

#### 7.2.6.1 IV Test

A fully assembled module also undergoes an IV test as described in [7.2.2](#). The primary purpose of this test is to ensure that no damage was caused to the circuitry during the assembly process and the module could be operated at high voltages. The IV result for a sample module is shown in figure [7.18](#). The operational range for this particular module is between -100 V and -400 V.



**Figure 7.18:** IV test for a fully assembly module.

#### 7.2.6.2 Pretest

It is composed of several subtests and its purpose is to check the basic functionalities of the ROCs and to calibrate some of the DAC [list of DAC here or in ch 2?](#) settings. A couple of these subtests are *ProgramRoc* and *SetVthrCompCalDel*. The *ProgramRoc*

measures the difference in current ( $I_{ana}$ ) drawn by the amplifiers when a voltage ( $V_{ana}$ ) is applied and remove. If the difference between these two measurements is non-zero it implies that we are able to change DAC values by sending a command, the ROC is programmable. This test is done for all 16 modules in a ROC. The *SetVthrCompCalDel* subtest is done to optimize the value of the VthrComp and CalDel DACs. It chooses a pixel from within a ROC and sends 5 calibration pulses to the PUC of this pixel. This process is repeated for the  $256 \times 256$  parameter space of these DACs and the response of the pixel is read to make an efficiency plot. Then VthrComp is set to the lower plateau plus 50 units and CalDel is set to half of the left and right edges. This is known as the *VthrComp* and *CalDel* working point of the pixel. Figure 7.19 shows the output of these subtests for a sample module

#### 7.2.6.3 Pixel Alive

In the pixel alive test three subtests are performed: *Alive test* checks for the response of a pixel by sending 10 calibration pulses (hits) to it and recording how many the pixel reports back. Pixel with 10 hits are marked as good, those with less than 10 hits are flagged as faulty, and those with zero hits are called dead. In the *Mask test* all pixels are disabled and the same efficiency measurement is done. Pixels with zero efficiency are marked as good while those with efficiency greater than zero are bad. The *AddressDecoding* test checks the specific address of the pixel within the ROC. If the response of the pixel does not match the address to which it was sent the pixel is marked as bad. repeats the same procedure but checks that the order of the resulting data. If the address of a given pixel is out of order, the recorded hit is given a negative pulse height value. Pixels with negative hits are flagged as faulty. Figure 7.20 shows the result of the pixel alive test for a fully working module and Figure 7.21 shows a module with faulty ROC and a ROC with faulty pixels.

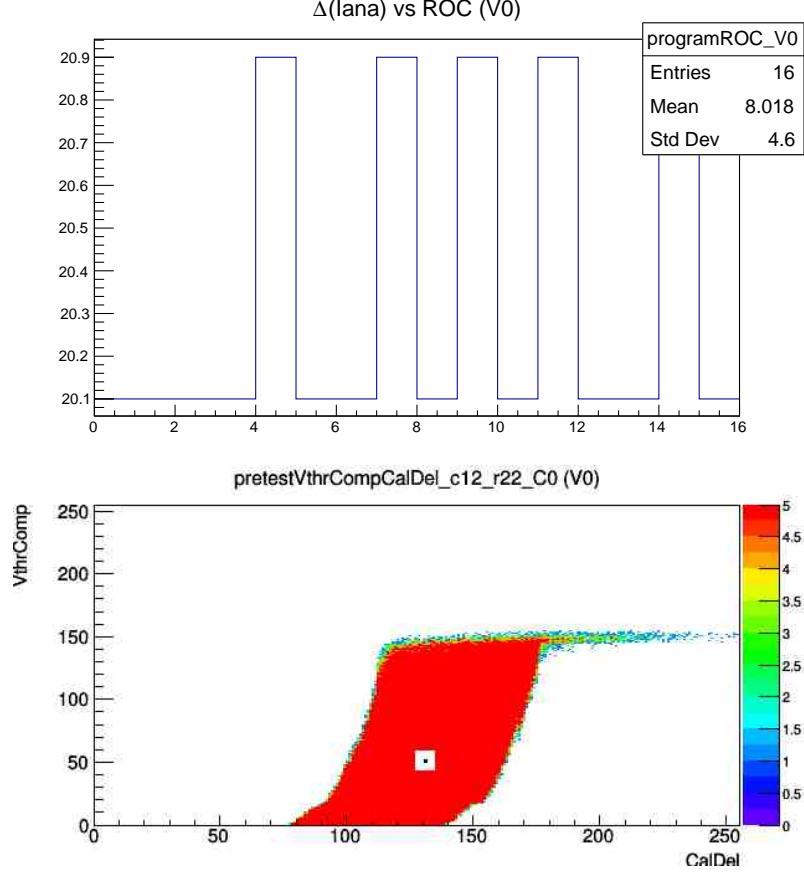


**Figure 7.19:** Output of the ProgramRoc (left) and finding working pixel (right) subtests.

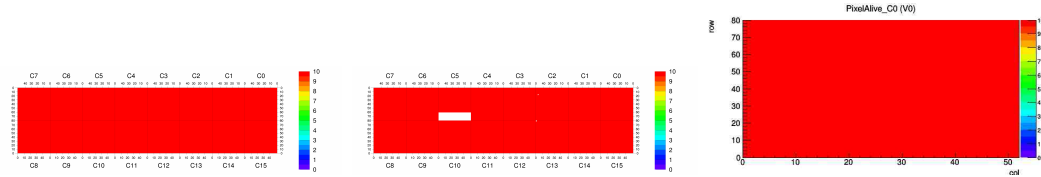


**Figure 7.20:** Pixel alive test for a fully assembled module. a) Alive test, b) Mask test, and c) AddressDecoding test.  
right fig

#### 7.2.6.4 Trimming Test

The aim of the the trimming test is to (calibrate) set the threshold of all pixel on a ROC as uniform as possible. It attempts to do this by varying the VthrComp, Vtrim, and Trim bits DACs. The Trimming test sets VthrComp and Vtrim for the entire ROC and then uses trim bits to further refined the threshold of individual pixels. After

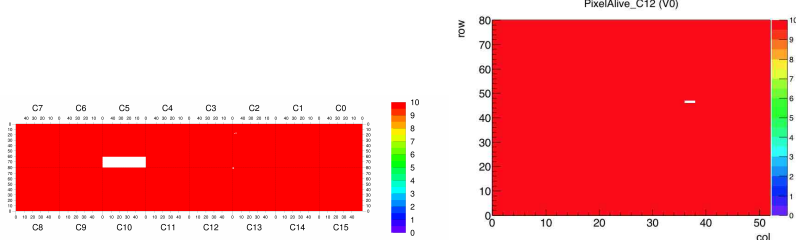


**Figure 7.21:** Pixel alive for a fully assembled module. a) a module with a faulty ROC and b) a ROC with faulty/dead pixels

the trimming test is finished all pixels within the ROC will have a threshold value as low as possible but still higher than the electrical noise. Furthermore, a TrimBits subtest verifies that all trim bits are working by sequentially enabling each bit and observing its effect on the pixel threshold distribution. The trimming test works as follows: first, with  $V_{cal}$  set to a target value, it finds the  $V_{thrComp}$  turn-on value by producing S-Curves for all pixels with respect to  $V_{thrComp}$ . Then,  $V_{thrComp}$  is set to the value of the pixel with the lowest turn-on value. A ROC map distribution of turn on values for a ROC can be seen in figure 7.22. Then, with the  $V_{thrComp}$  set to its lowest value, the test tries to minimize the  $V_{trim}$  value by repeating the previous process and finding the pixel with the highest  $V_{cal}$  turn-on value, see Fig 7.22. This is the pixel that requires the most trimming to have its  $V_{cal}$  threshold reduced to the target value. Following, with all trim bits enabled, the test performs an efficiency scan over  $V_{trim}$  and  $V_{cal}$  DACs 7.22 to find the value of  $V_{trim}$  that corresponds to a turn-on at the target  $V_{cal}$ .

Next, starting from a high  $V_{trim}$ , its value is iteratively lowered until the  $V_{cal}$  turn-on surpasses the target  $V_{cal}$ , which corresponds to the minimum value that can trim this pixel. This is the final value of the  $V_{trim}$  DAC for the the ROC. Finally, with the values of the  $V_{thrCaomp}$  and  $V_{trim}$  set, the test refine the threshold on each pixel by modifying the 4 Trim bits. Starting with the Trim bits set to 7 [0111], scurves

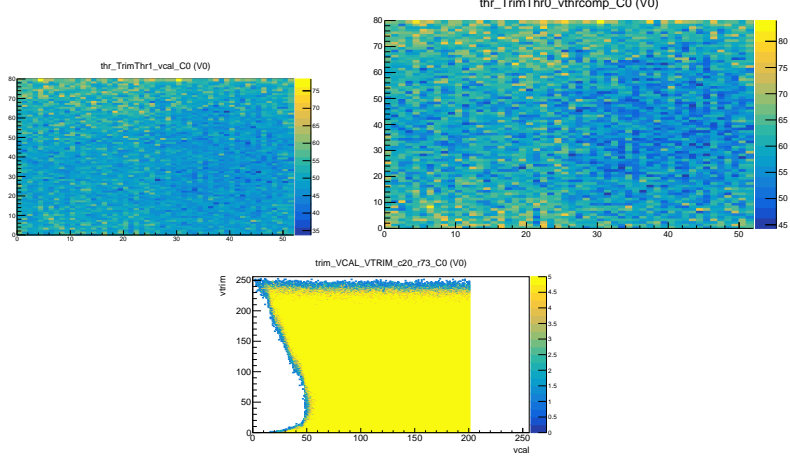


**Figure 7.22:** Trim test optimization for. left: Vcal turn on, center: Vthr turn on, right: efficiency in the Vtrim-Vcal plane.

are used to find the Vcal turn-on value. If the pixel **reports a hit** fires below (above) the target Vcal value, the Trim bits value is increased (decreased) by 4, so that the amount of trimming is decreased (increased). This process is repeated three more time increasing or decreasing the Trim bits values by 2, 1, and 1 unit respectively, covering the full range, 0-15, of the Trim bits. Figure 7.23 shows a ROC map of Vcal for Trim bits = 7 and after 4 corrections are made and the final Vcal map and distribution could be seen in figure 7.24.

#### 7.2.6.5 PH Optimization

The PHOptimization test is responsible for setting the dynamic range of the output pulse height (PH) as calculated by the ADC serializer. It accomplishes this by optimizing the *PHOFFSET* and *PHSCALE* DACs, which adds a constant offset to the pulse height measurement and sets the gain of the ADC. *PHOptimization* works in the following way: First it identifies a low gain and a high gain ensuring it is working (good in pixel alive) and as far as possible from the edges of the sensor. Then, two Vcal signals, low = 60 and high = 255, are sent to each pixel in a ROC and 1D distribution

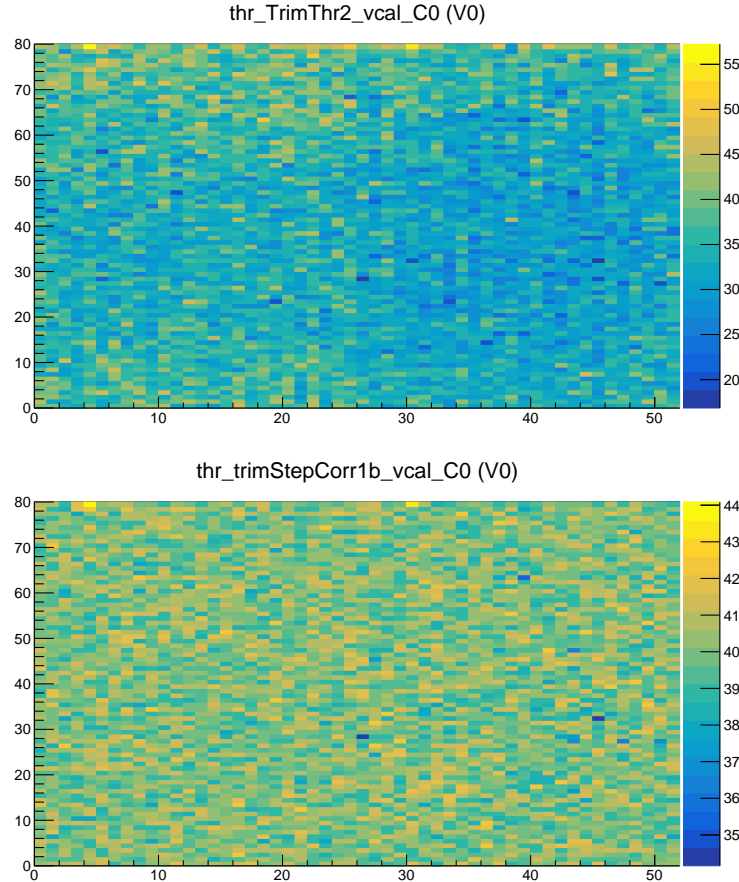


**Figure 7.23:** Trim bits map distributions for the Vcal turn-on values for the initial and final Trim bits values.

of the PH is created for each vcal value, see figure 7.25. A pixel close to the center in each of these distribution is selected as the low and high gain pixel for that ROC.

After both pixels have been identified the test optimizes  $PHScale$  and  $PHOffset$  by performing a 2D scan over these two DACs plane. The output of these scan is showing if figure 7.26. The final value of the DACs are chosen from the interception of these two plots as showing in figure 7.26c.

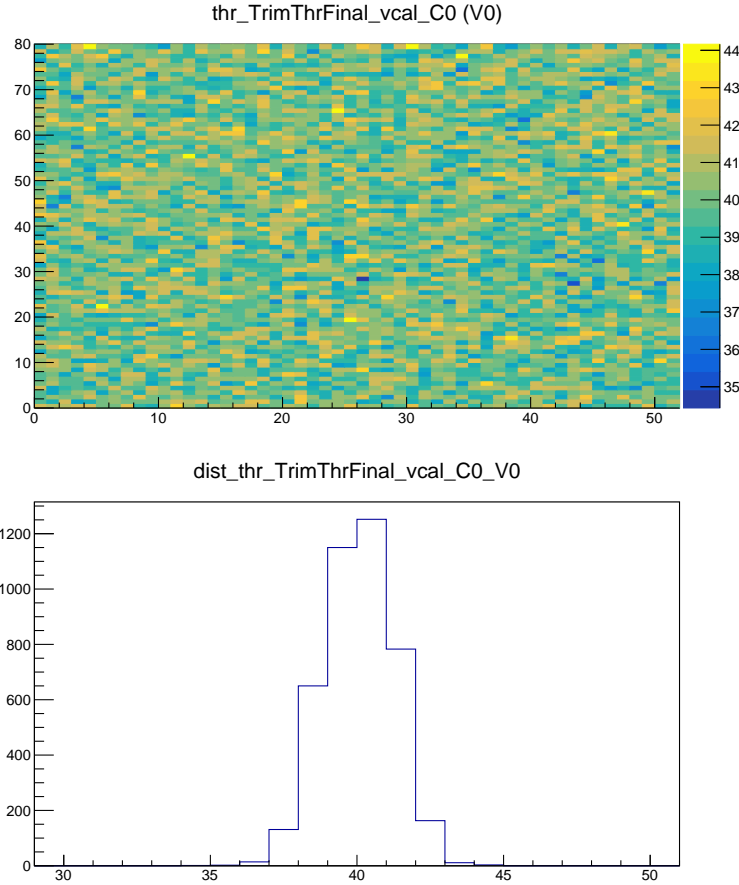


**Figure 7.24:** Final map and distribution of Vcal threshold after the Trim test have finished.

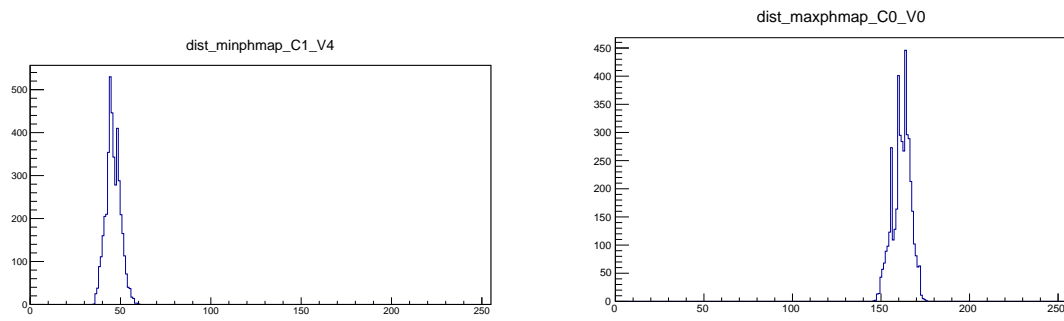


**Figure 7.25:** Distribution of PH as a function of Vcal used to indentify low (top or left) and high (bottom or right) gain pixels.

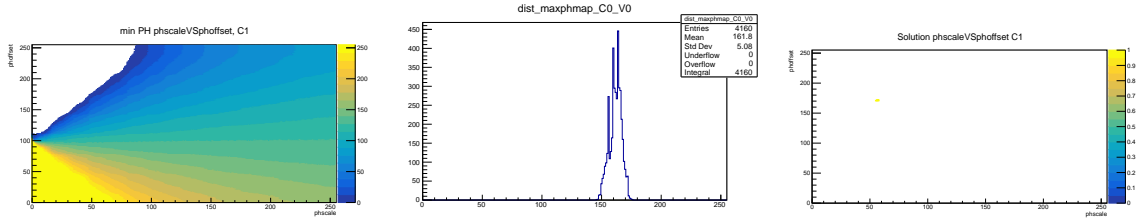


**Figure 7.26:** Scan on the PHOffset-PHScale plane used to optimize these DACs. a) for a low gain pixel, b) for a high gain pixel, c) interception of a) and b) showing the values of PHOffset and PHScale.

### 7.2.6.6 Gain Pedestal

The *Gainpedestal* test measures and records the variation in gain for each pixel in a ROC. Since each pixel will have a different gain these values are needed to calibrate the PH to an input signal. It produces a PH vs. Vcal curve and fits it with an error function recording the its 4 parameters. Parameter 0 corresponds to the Vcal value at the center of the error function. Parameter 1 is proportional to the width of the turn-on and is therefore inversely related to the gain of the pixel. Parameter 2 shifts the error function upwards, with a value of unity moving the floor of the function to zero. Parameter 3 corresponds to half the height of the function, and should be near 127.5 (255/2). [include equation?](#) The test also measures the linearity of the pixel response by comparing the integral of the fitted error function in the vcal range to a linear approximation. The results of the test for parameter zero and its linearity are shown in figure 7.27.

### 7.2.6.7 Scurve Test

The SCurve test measures the efficiency of a pixel as a function of Vcal. It is based on the assumption that a pixel will not respond to lower values of Vcal but it will always respond for higher values. In the absence of noise this curve will be just a step function which changes from zero effiecinecy below the threshold to a region of 100%

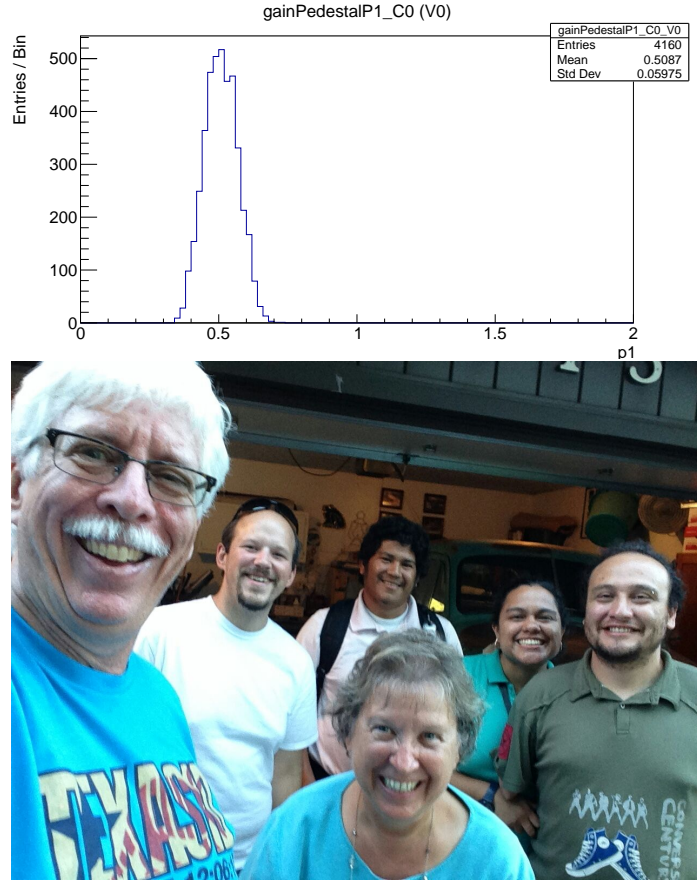


**Figure 7.27:** Results of the *GainPedestal* test. a) parameter 0 and b) linearity test [find figure](#)

efficiency above. The effect of the noise is to smear out the step function giving it a *S* shape. As the noise is assumed to follow a Gaussian distribution, the SCurve if fitted with an error function and its width is a measure of the noise level in the pixel. Since the Vcal is known at this point in the testing procedure the SCurve is done around this Vcal value. In order to extract an accurate estimate of the width the number of triggers used for the test is 200. The output of this test can be seen in figure ??

#### 7.2.6.8 Bond Bonding Test

could be better, include the ROC-Sensor air gap? The primary purpose of the *Bump-Bonding test* is to identify problems with the bumps connecting the sensor to the

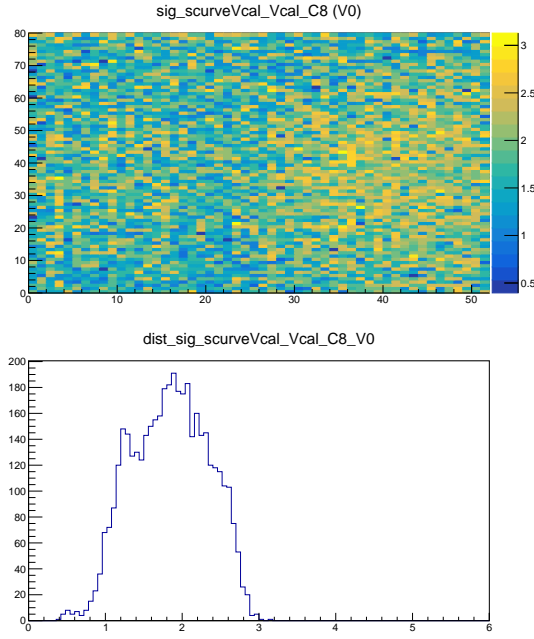


**Figure 7.28:** Left: ROC map of the Vcal s-curve turn-on widths. Right: 1D distribution of the vcal scurve width.

ROC. The test works by a calibration signal to the sensor via the alternatively path labeled 'sensor calib' [7.32](#). The signal then reaches the sensor and makes its way to the ROC via the bump bond where it can be normally read. The strength of the signal is measure and compare to the one sent. In the *pXar* software usually 5 signal of 250 Vcal units are sent to each pixel during a *BumpBonding* test. The **output** of the test is shown if figure [7.29](#)

#### 7.2.6.9 Summary

The UNL-HEP module production was a susceesful **project** that culminated with the production and testing of over 500 modules. Figure [7.30](#) shows the module production over time for both assembly sites, UNL and Purdue University. Production started slow for the first two months but ramped up after fixing some issues with the parts. Besides that the other time when production almost stopped was around July of 2016

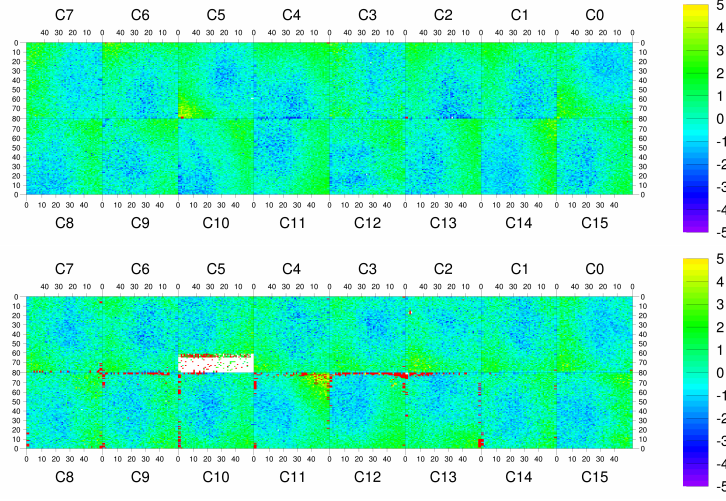


**Figure 7.29:** Bond bonding test.

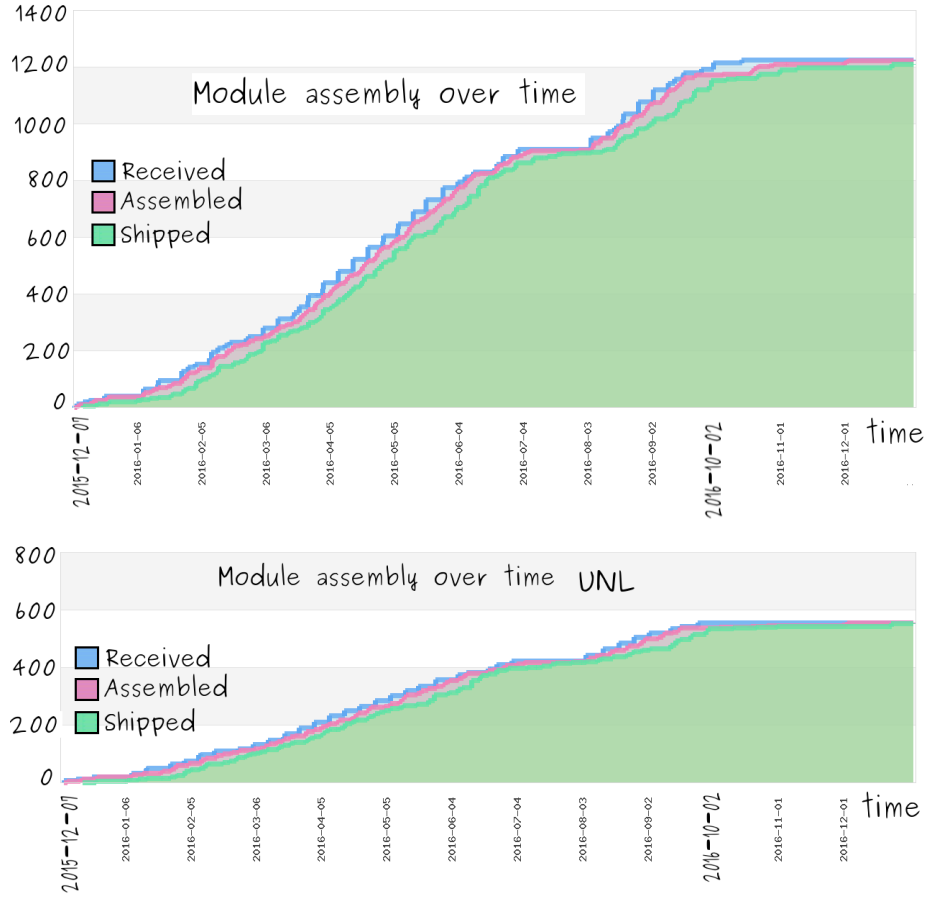
Grade	$I(V=-150V)$	$I(V=-150V)/I(V=-100V)$	Pixel defects
A	$< 2\mu A$	$< 2$	$< 1\%$
B	$< 10\mu A$	$< 2$	$< 4\%$
C	$> 10\mu A$	$> 2$	$> 4\%$

**Table 7.1:** Module grades for the Fpix phase I module production.

when the BBM provider had difficulties and could not supply BBMs on time. [include purdue database](#)

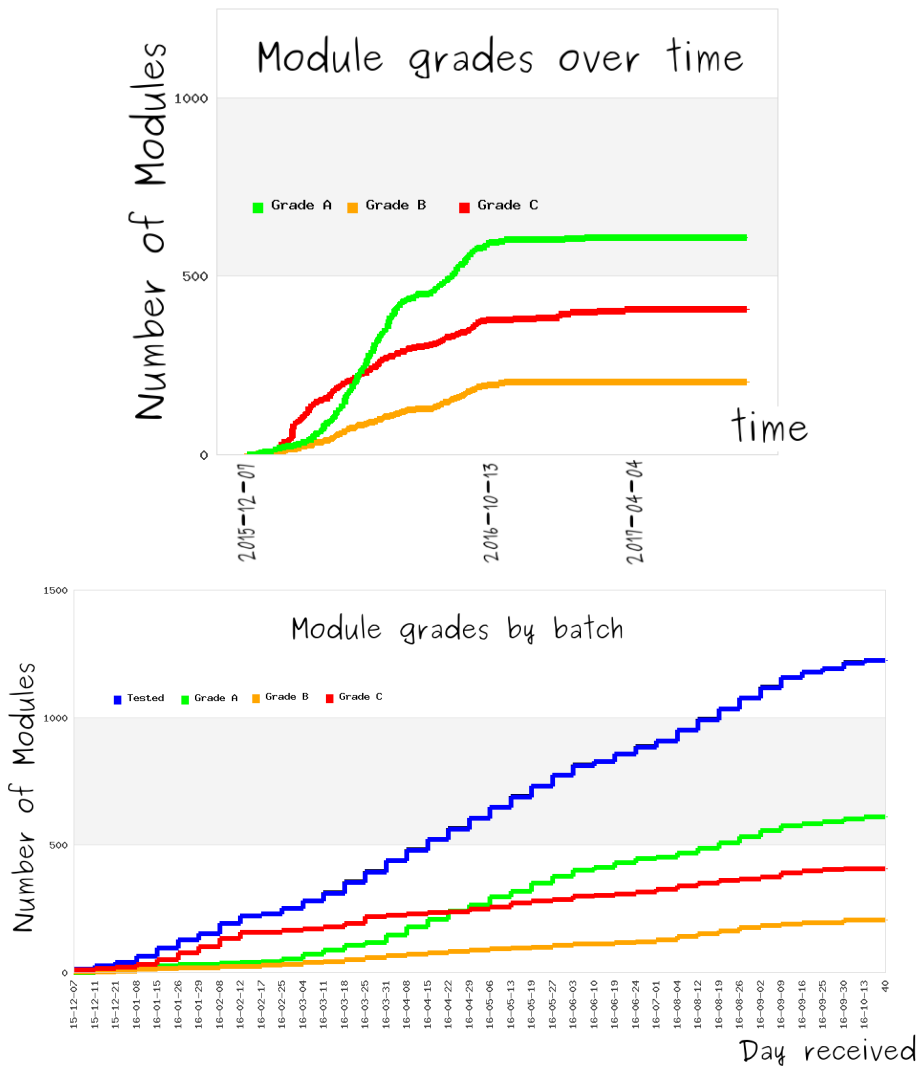
Following the production and testing these of modules a grading scheme was adopted. The grade of a module was given based on the amount of current drawn by it at nominal operating voltages and the number of pixel defects. UNL graded modules at  $17^{\circ}C$  but the final grade of the modules was given at FermiLab, where the *Fulltest* was done at  $-10^{\circ}C$ . Table 7.1 shows the grade names and the requirements a module needs to meet to obtain this grade. Since there are 672 modules needed to populate the forward part of the pixel detector and there were not enough grade A modules, some parts of the outer most cylinder was populated with grade B modules.

Figure 7.31 shows graded modules over time as well as the module grading by batch received and tested at FermiLab. The integration of the modules into the



**Figure 7.30:** Module assembly over time for both assembly sites (top) and for UNL (bottom).

half cylinders was done at FermiLab, they were later transported to Switzerland and installed into the CMS detector.



**Figure 7.31:** Module grade over time (top) and per received batch at the integration site (bottom).

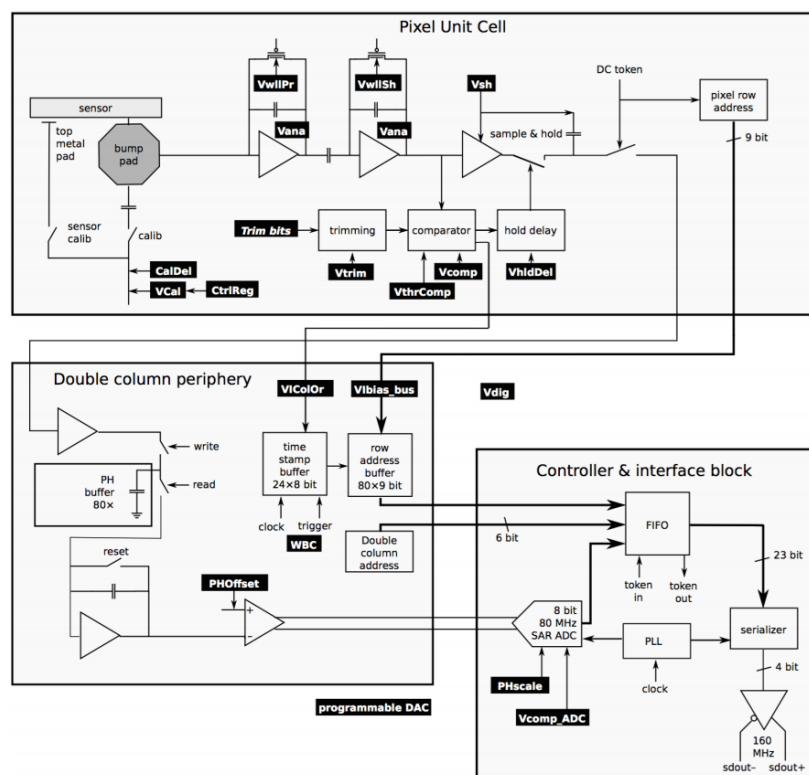


**Figure 7.32:** A schematic view of a pixel circuit showing the PUC, CIB, DCP, and some of the relevant DACs.

## CHAPTER 8

---

### Beam Test of the RD53 chip for CMS Pixel Detector Upgrade Phase 2

---

la verdad es que

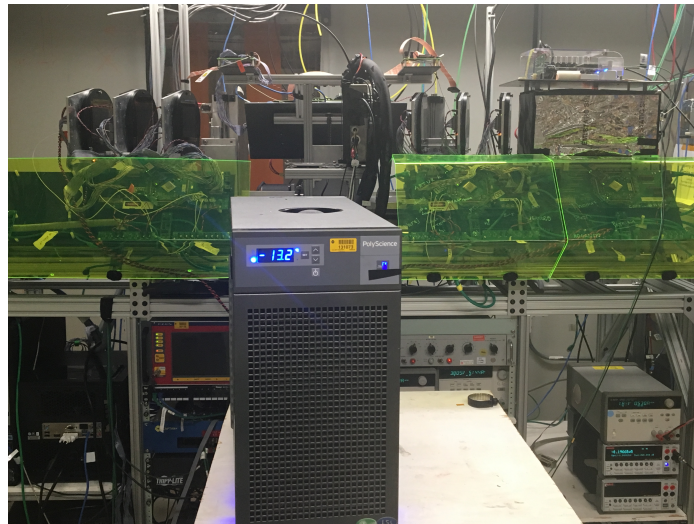


**Figure 8.1:** Test beam setup.

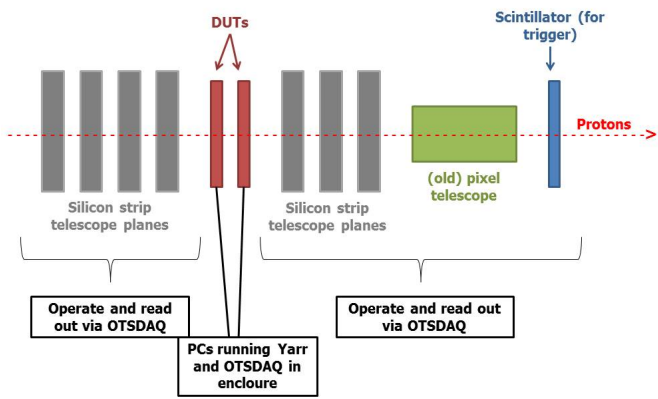


**Figure 8.2:** Test beam setup.

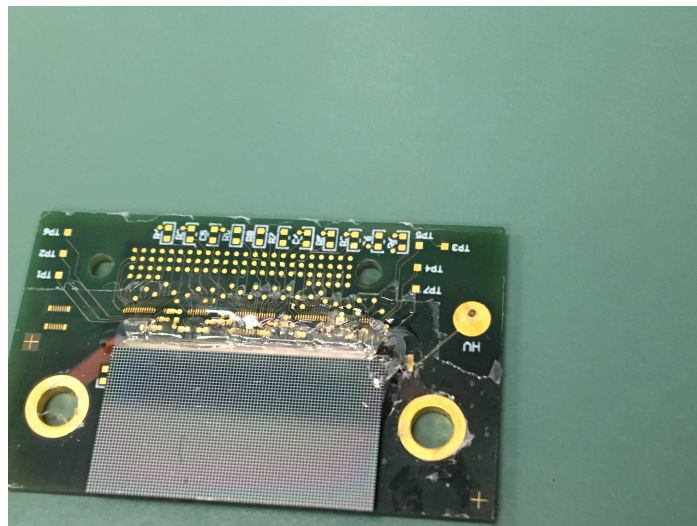


**Figure 8.3:** Chip.

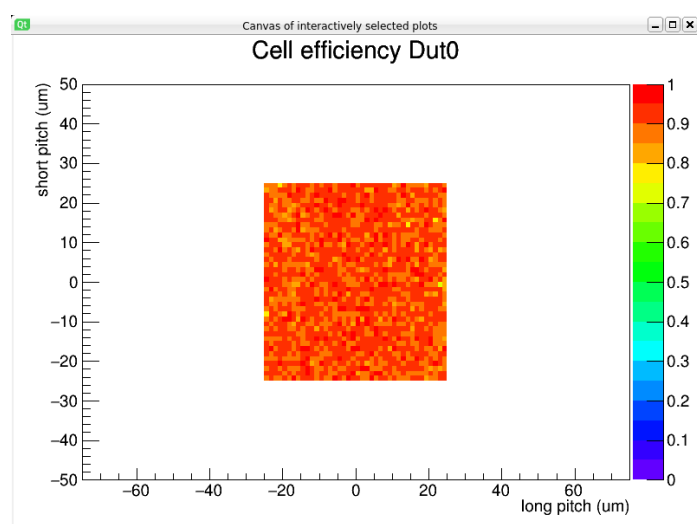


**Figure 8.4:** Cell efficiency.

## CHAPTER 9

---

### Conclusions

---

#### **9.1 Analysis**

#### **9.2 Phase 1**

#### **9.3 Beam Test**

---

## References

---

- [1] Evans, Lyndon, (ed. ) and Bryant, Philip, (ed. ), LHC Machine, JINST 3 (2008) S08001 <https://iopscience.iop.org/article/10.1088/1748-0221/3/08/S08001>
- [2] P. Higgs. Broken Symmetries and the masses of gauge bosons. <https://journals.aps.org/prl/pdf/10.1103/PhysRevLett.13.508>
- [3] P. Higgs. (1964). "Broken Symmetries and the Masses of Gauge Bosons". Physical Review Letters. 13 (16): 508–509. Bibcode:1964PhRvL..13..508H. doi:10.1103/PhysRevLett.13.508
- [4] Englert, F.; Brout, R. (1964). "Broken Symmetry and the Mass of Gauge Vector Mesons". Physical Review Letters. 13 (9): 321–323. Bibcode:1964PhRvL..13..321E. doi:10.1103/PhysRevLett.13.321.
- [5] Brout, R.; Englert, F. (1998). "Spontaneous Symmetry Breaking in Gauge Theories: A Historical Survey". arXiv:hep-th/9802142.
- [6] ATLAS Collaboration, "Observation of a new particle in the search for the Standard Model Higgs boson with the ATLAS detector at the LHC", Phys. Lett. B 716 (2012) 1, doi:10.1016/j.physletb.2012.08.020, arXiv:1207.7214.

- [7] CMS Collaboration,  $\rightarrow$ IJObservation of a new boson at a mass of 125 GeV with the CMS experiment at the LHC $\rightarrow$ , Phys. Lett. B 716 (2012) 30, doi:10.1016/j.physletb.2012.08.021, arXiv:1207.7235.
- [8] The Atlas collaboration, Technical Design Report LHCC 99-14, ATLAS TDR 14. CERN, Geneva Switzerland, 1999
- [9] CMS Collaboration. The CMS Experiment at the CERN LHC. Volume 3, 2008.
- [10] LHCb Collaboration, S. Amato et al., LHCb technical proposal,CERN-LHCC-98-04
- [11] ALICE: Technical proposal for a large ion collider experiment at the CERN LHC, CERN-LHCC-95-71.
- [12] from <https://videos.cern.ch/record/1610170>.
- [13] CMS, the Compact Muon Solenoid: Technical proposal CERN-LHCC-94-38.
- [14] <http://cms.web.cern.ch/news/cms-detector-design>
- [15] <https://cms.cern/news/first-measurement-lhc-run-2-pp-data-collected-2016-2017>
- [16] A. Dominguez et. al. “CMS Technical Design Report for the Pixel Detector Upgrade”, CERN-LHCC-2012-016. CMS-TDR-11.
- [17] UNL Phase I FPIX Assembly Standard Operating Procedures. From <https://github.com/psi46/unl-sop>, 2016.
- [18] J. Monroy. Search for production of a Higgs boson and a single top quark in multilepton final states in pp collisions at  $\sqrt{s} = 13$  TeV July 2018.
- [19] F. Meier “ Forward Pixel Module Glueing at UNL” YouTube, Sep. 15, 2014, from <https://www.youtube.com/watch?v=ofdntTIwKY4>.

- [20] Aerotech (n.d). “AGS15000 Series”, from <https://www.aerotech.com/product-catalog/gantry-system/ags15000.aspx?p=%2fproduct-catalog%2fgantry-system.aspx%3f>
- [21] J. Monroy (n.d). Home [YouTube Channel]. from <https://www.youtube.com/channel/UCi7S7vhYpieL0y2KJ0SS0eg>.
- [22] pXar software framework 2015, from <https://twiki.cern.ch/twiki/bin/viewauth/CMS/Pxar>.
- [23] J. Antonelli. “FPix Module Testing Reference Guide”, Sep. 2015, from <https://cms-docdb.cern.ch/cgi-bin/DocDB/RetrieveFile?docid=12690&filename=fpix-module-testing-reference-guide.pdf&version=5>
- [24] Photograph courtesy of Brian Farleigh, 2020.